Research Square

Preprints are preliminary reports that have not undergone peer review.
They should not be considered conclusive, used to inform clinical practice,
or referenced by the media as validated information.

Integrated multi-omics reveal retinal photoreceptors initiating liver-brain-retina axis dysfunction in depression

Yuan-Hong Deng
Chengdu University of Traditional Chinese Medicine
Yue-Chi Chen
Chengdu University of Traditional Chinese Medicine
Xin-Yan Yang
Chengdu University of Traditional Chinese Medicine
Da-Neng Wei
Chengdu University of Traditional Chinese Medicine
Jia-Le Xiong
Chengdu University of Traditional Chinese Medicine
Meng-Yao Wang
Chengdu University of Traditional Chinese Medicine
Jia-Li Zeng
Chengdu University of Traditional Chinese Medicine
Ying Xie
Chengdu University of Traditional Chinese Medicine
Huan Zhou
Chengdu University of Traditional Chinese Medicine
Shu-Yu Wang
Chengdu University of Traditional Chinese Medicine
Jian-Tao Song
China Academy of Chinese Medical Sciences
Yong Tang
Chengdu University of Traditional Chinese Medicine
Ya-Fei Zhao
zhaoyafei@cdutcm.edu.cn

Chengdu University of Traditional Chinese Medicine

Article

Keywords: retinal photoreceptors, depression, bile secretion, integrated multi-omics, OPCs

Posted Date: November 26th, 2026

DOI: https://doi.org/10.21203/rs.3.rs-11644756/v1

License: This work is licensed under a Creative Commons Attribution 4.0 International License.
Read Full License

Additional Declarations: No competing interests reported.

Abstract

Retinal abnormalities have been recognized as promising accessible biomarkers for depressive pathogenesis, the mechanistic link between peripheral metabolic dysfunction and concurrent retinal and brain pathological changes in depression remains largely unelucidated. Here, we integrate retinal phenotyping, proteomics, metabolomics, single-cell transcriptomics and behavioral assays to delineate a liver-brain-retina signalling axis driving chronic stress-induced depression. We show that retinal photoreceptors (rod and cone PRs) exhibit selective vulnerability to chronic stress, constituting the key cellular substrate driving retinal remodelling under stress conditions. Multi-tissue omics analyses further demonstrate that chronic stress disrupts hepatic bile secretion, which perturbs bile acid-associated signalling in retinal rod photoreceptors and prefrontal cortical oligodendrocyte precursor cells, with Abcb1a and VPS26b as candidate molecular correlates governing this multi-organ cross-talk. Pharmacological restoration of hepatic bile acid homeostasis via FXR agonist treatment rescues stress-induced depressive-like behaviours and retinal pathological abnormalities in mice. Collectively, our findings identify hepatic bile acid signalling as a critical systemic regulator of depression-related retinal and cortical dysfunction, and highlight photoreceptor vulnerability as an early cellular hallmark of stress-triggered neuroretinal impairment.

1. Introduction

The retina serves as a unique and accessible interface linking peripheral physiological states to the central nervous system (CNS), offering direct, non-invasive readouts of neuronal and vascular perturbations linked to systemic diseases. As an embryonic derivative of the diencephalon, the retina retains conserved developmental and immune features with the brain [1]. Retinal ganglion cells (RGCs) establish functional projections to diverse brain regions governing circadian rhythm modulation, sensory signal processing and emotional homeostasis [2], while metabolic regulation, immune responses and humoral signaling pathways further constitute bidirectional crosstalk between the eye and brain[3, 4]. Collectively, these anatomical and functional properties render retinal abnormalities promising surrogate biomarkers for diagnosing and monitoring CNS pathological changes.

Mounting clinical evidence has validated consistent retinal structural and functional aberrations in major depressive disorder (MDD). Patients with depression exhibit reduced thickness of the retinal nerve fiber layer (RNFL) and total retina, altered retinal vascular morphological parameters, and deficient electroretinographic responses, with such retinal deficits tightly correlated with the severity of depressive symptoms [5–8]. Furthermore, the mood-modulating effects of light therapeutic interventions underscore how retinal signaling, mediated by the retina–ventral lateral geniculate nucleus (vLGN)–dorsal raphe nucleus (DRN) pathway, plays a critical role in regulating neuroendocrine activity and circadian homeostasis [9–14]. Nevertheless, the specific retinal cell subtypes vulnerable to depressive pathology and the upstream systemic mechanisms driving retinal dysfunction in MDD remain largely uncharacterized.

The liver is a core effector of systemic metabolism, endocrine signaling and immune homeostasis, and its regulatory role in neuropsychiatric pathogenesis has garnered increasing recognition [15]. The functional liver–brain axis is well-documented in the context of hepatic encephalopathy, and accumulating preclinical and clinical evidence further demonstrates that liver-derived circulating factors modulate stress-associated behaviors and depressive phenotypes[16–18]. Notably, the liver also engages in interorgan communication with the retina via shared metabolic and inflammatory signaling networks. In multiple metabolic disorders, hepatic dysfunction is closely coupled with retinal microvascular damage and neuronal degeneration, and retinal phenotypic alterations can faithfully reflect systemic metabolic stress originating from hepatic dysregulation[19–23]. These empirical findings support the hypothesis that hepatic metabolic remodeling may mediate synchronized functional and structural dysfunction in the retina and brain under chronic stress conditions.

Despite these pivotal advances, it remains elusive whether chronic stress and depression trigger coordinated pathological alterations across the liver, retina and brain axis. Existing studies have predominantly focused on pairwise organ interactions, resulting in a poorly defined landscape of systemic interorgan crosstalk spanning these three key organs. To address this critical research gap, the present study integrates behavioral phenotyping, in vivo retinal imaging, proteomic, transcriptomic and metabolomic profiling in a chronic restraint stress (CRS) mouse model. By systematically profiling molecular perturbations across the liver, peripheral circulation, retina and prefrontal cortex, this study aims to identify key cellular populations and conserved systemic metabolic pathways driving stress-induced retinal and prefrontal cortex (PFC) dysfunction, and further elucidate their potential functional mechanisms underlying depressive-like pathogenesis.

2. Materials and Methods

2.1 Animals/Mice

All experiments were conducted on male mice aged 8-16weeks WT C57BL/6J mice. Mice were housed in a specific pathogen-free facility on a 12-h light-dark cycle with ad libitum access to food and water. All experimental procedures were conducted in accordance with the National Institutes of Health Guide for the Care and Use of Laboratory Animals, and approved by the Animal Care and Use Committee of Chengdu University of Traditional Chinese Medicine (No. 202601052).

2.2 Chronic restraint stress

CRS was performed in a specially customized tube. Mice were restrained horizontally in tubes for 3h in the first 7 days and for 6h in the next 7 days. The unstressed mice were no treated [24, 25].

2.3 Behavior Test

Sucrose preference test (SPT)

Before the formal testing, mice were housed individually and habituated with 2 identical bottles of 2% sucrose and water for 24h, in order to prevent possible side preference in the teat, the position of bottles were changed for 12h. Then the experimental mice were water and food deprived for 12h. mice were tested to drink from two bottles for 12h. The consumption of water, sucrose solution, and total intake of liquids were assessed in all groups. The preference for sucrose was determined by quantifying the ratio between the sucrose solution consumed and the overall liquid intake.

Tail suspension test (TST)

The mice were individually wrapped with tape at approximately 1cm from the end of the tail. The mice were then fixed upside down on a horizontal bar with the nose tip about 30cm above the ground. Animal behaviors were recorded for 6min and the immobility time was scored during the last 5min.

Forced swimming test (FST)

Mice were gently placed in a glass cylinder (height, 30 cm; diameter, 20 cm; water level, 15 cm) for 5 min. Animal behaviors were recorded for 6min and the immobility time was scored during the last 5min.

Open field test (OFT)

OFT was conducted to evaluate the depressive like behavior. The apparatus consisted of a rectangular chamber (50×50×50 cm) made of white, high density, non-porous plastic. Mice were gently placed in the center of the chamber and their motility was recorded for 10 min. The total running distance, and the time and distance in the center versus the periphery of the open field chamber were recorded by an automated video tracking program (EthoVision XT 9.0; Noldus, Wageningen, The Netherlands).

2.4 Optical coherence tomography (OCT)

After satisfactory anesthesia, the pupils were dilated using 1% atropine. A viscoelastic agent was applied to the eyes of the mice to prevent dehydration. Using Phoenix Image-guided OCT (Phoenix Technology Group, Pleasanton, CA, USA), the mice were placed on a bracket. The lens was aimed at the eyeball and slowly approached; the angle was carefully adjusted to place the eyeball at the center of the lens. After adjusting the gamma value, OCT images of the optic nerve and surrounding area were obtained. Retinal layer segmentation was performed with InSight software (version v2.1.7237).

2.5 Hematoxylin and eosin (HE) staining

Eyeballs were fixed in 4% paraformaldehyde (PFA) and underwent serial sectioning (3 μm in thickness) using a sagittal approach that traversed through the optic nerve head. These sections were then subjected to HE staining. Retinal morphology images were captured using a light microscope. The measurement of retinal thickness occurred at intervals of 400 μm from the optic nerve head, facilitated by SlideViewer software. Cell nuclei in the outer nuclear layer (ONL) and total retinal thickness were counted using ImageJ software.

2.6 Cell dissociation of the retina tissues for Single-cell RNA-seq(scRNA-seq)

As previously research [26], detached retinal cells were obtained. Breifly describing as following, the retina tissues were transfered in MACS Tissue Storage Solution (Miltenyi Biotec, cat. no. 130-100-008) and placed on ice. Added 2 ml 37°C preheated digestion solution (Miltenyi Biotec, cat. no. 130-095-929) into retina tissues, 37°C water bath, Enzymatic incubation time was about 45 min. After incubation finished, 10% FBS (Pricella, cat. no.164210-50) was added and the solution was filtered using a 40-μm cell strainer (Corning, cat. no. CLS431750). The suspensions were centrifuged at 300 g for 3 min at 4°C, and remove the red blood cells (Roche, cat. no. 11814389001). The suspensions were centrifuged at 300 g for 3 min at 4°C, and the pellets were resuspended in PBS with 0.01% Bovine serum albumin (Sigma, cat. no. A1933). The final cell suspension was stained with trypan blue and live cells were counted using Countess II FL Automated Cell Counter (Thermo Fisher scientific, USA).

2.7 Cell nucleus extraction of the PFC tissues for Single-cell RNA-seq

As previously describing [27], the PFC tissue cell nucleus extraction was carried out accordance with the instructions of the kit (MobiDrop (Zhejiang) Co., Ltd., cat. no. Mobisolution V2.3). The frozen PFC tissues were placed in 1.5 mL centrifuge tube pre-chilled on ice and add 500 μL of pre-chilled homogenization Buffer with 1× protease inhibitor cocktail (Roche, cat. no. 4693132001 and 0.4 U/μl RNase inhibitor (Invitrogen™, cat. no. 10777019) and cut it into small pieces about 1mm in diameter with surgical scissors. Then, carry out the organization and grinding process and transfer both tissue fragments and liquid together into the pre-chilled tissue grinder using a pipette. Allow the mixture to stand for 5 minutes to ensure thorough tissue saturation. Grind the tissue fragments vertically using pestle until a noticeable reduction in resistance is observed (approximately 10–15 strokes). Avoid rotating the pestle during grinding to prevent nuclear degradation. In the grind process, pipette 10 μL of homogenate, mix with 10 μL of AO/PI dye, and assess tissue dissociation adequacy and estimate nuclear yield with Countstar cell counter. The purification of the cell nucleus was carried out according to the previous method. Finally, dilute nuclei to a concentration of 1,000–2,000/μL for single-cell sequencing applications.

2.8 ScRNA-seq library preparation and sequencing

Then 36,000 cells or cell nucleus were loaded into microfluidic chip of Chip A Single Cell Kit v2.1 (MobiDrop (Zhejiang) Co., Ltd., cat. no. S050100301) to generate droplets with MobiNova-100 (MobiDrop (Zhejiang) Co., Ltd., cat. no. A1A40001). Each cell was involved into a droplet which contained a gel bead linked with up to millions oligos (cell unique barcode). After encapsulation, droplets suffer light cut by MobiNovaSP-100(MobiDrop (Zhejiang) Co., Ltd., cat. no. A2A40001) while oligos diffuse into reaction mix. The mRNAs were captured by cell barcodes with cDNA amplification in droplets. Following reverse transcription, cDNAs with barcodes were amplified, and a library was constructed using the High Throughput Single-Cell 3' Transcriptome Kit v2.1 (MobiDrop (Zhejiang)Co., Ltd., cat. no. S050200301)

and the 3' Dual Index Kit (MobiDrop (Zhejiang) Co., Ltd., cat. no. S050300301). The resulting libraries were sequenced on an DNBSEQ-T7.

2.9 Single-cell 3’ transcriptome data process and analysis

Raw data (fastq format) of single-cell 3’ transcriptome was pre-analyzed by MobiVision (version 3.0, MobiDrop), and reads were aligned to Mus musculus reference GRCm39. Filtered cell-gene matrix was obtained with MobiVision. For further analysis, low-quality cells were filtered out according to the methods of disclosure. The original data, after quality control, retain high-quality single-cell data for downstream analysis: at the gene level, only genes expressed in at least 3 cells are retained, and at the cell level, cells with a detected gene number greater than 200 are retained. The proportion of mitochondrial genes is set at 0.10 in brain tissue samples, 0.20 in retinal samples, 0.01 for hemoglobin genes, and 0.60 for ribosomal genes. After log10 transformation of nCount (total UMI count) and nFeature (detected gene number) for each sample, outlier cells located beyond the median ± 3 times the standard deviation is excluded.

The quality-controlled data are normalized and dimensionally reduced clustered in the R environment based on the Seurat package (v 5.3.0) [28]. DoubletFinder (v2.0.6) [29] is used to find and eliminate double cells. Harmony (v1.2.3) [30] is used for batch effect correction across samples. Marker genes of each cell cluster are identified by the FindMarkers function. Cell annotation is completed using SingleR [31] automatic annotation combined with manual Marker annotation based on literature and CellMarker/PanglaoDB [32] databases.

To compare the gene expression differences of different cell types under different conditions at the population level, the pseudo-bulk strategy is adopted: the original UMI counts of the same cell type in the same biological sample are aggregated (aggregate) to form a sample-level expression matrix. DESeq2 (v1.48.2) [33] is used for differential expression analysis, with the screening criteria of $p < 0.05$ and $|log2FC| > 1$. The obtained differentially expressed genes are further subjected to ORA enrichment analysis.

2.10 Proteome sample preparation and LC-MS/MS analysis

As previous research methods, protein extraction and enzymatic digestion of liver, FC, and retina were performed. Meanwhile, based on previously described, the plasma protein was extracted, and the Albumin and IgG were removed by the Albumin/IgG Removal Kit (Cat No. P2295M, Beyotime) as the manual described. And then, the protein concentration was determined with a BCA kit (Cat #23225, Thermo). And then, precipitated protein with TCA (final concentration of 20% v/v). and collected protein via centrifugation (4,500g, 5 min, 4°C). Subsequently, the precipitated protein was washed with pre-cooled acetone, reduced by dithiothreitol (Cat No. 647563, Sigma), and alkylated with iodoacetamide (Cat No. A3221-1VL, Sigma). Subsequently, the protein sample was then diluted by adding 100 mM TEAB (Sigma) to a urea concentration of less than 2M. Then, the samples were centrifuged at 4°C for 30 min at

14,000 g, the supernatant was removed and the precipitate was redissolved with ammonium bicarbonate. Finally, trypsin (Promega, USA) was added (enzyme protein ratio 1:50) in the protein for the first digestion overnight and 1:100 trypsin-to-protein mass ratio for a second 4 h-digestion at 37°C. For each sample, 500 nL of total peptides were separated and analyzed with a nano-UPLC (Vanquish neo) coupled to Astral instrument (Thermo Scientific) with a nano-electrospray ion source. Separation was performed using a reversed phase column (EASY-Spray ™ HPLC (150 μm × 15 cm), Thermo Scientific, USA). Mobile phases were H_2O with 0.1% FA (phase A) and 80% ACN with 0.1% FA (phase B). Data independent acquisition (DIA) was performed in profile and positive mode with Orbitrap analyzer at a resolution of 240K and m/z range of 380–980 for MS1; For MS2 m/z range of 150–2000, Absolute AGC Value: 5E4, Maximum Injection Time: 3 ms. The HCD with normalized collision energy (NCE) of 25% and isolation window of 2 m/z.

2.11 Proteome data search and biological analysis

DIA raw data MS files were processed using DIA-NN software (2.2.0) [34]. The parameter setting as following, Carbamidomethyl [C] as a fixed modification, Oxidation (M) andd Acetyl (Protein N-term) as variable modifications. Trypsin was used as proteases. A maximum of 2 missed cleavage(s) was allowed. The false discovery rate (FDR) was set to 0.01 for both PSM and peptide levels. Peptide identification was performed with an initial precursor mass deviation of up to 4 ppm and a fragment mass deviation of 10 ppm. All the other parameters were reserved as default. Furthermore, functional annotation and analysis of identified proteins was performed based a suite of specialized tools: InterProScan for Gene Ontology (GO) [35] annotation; KofamKOALA (Version 1.3.1) [36] for KEGG pathway annotation; EggNOG-mapper (Version 2.1.12) for EggNOG functional classification; DIAMOND (Version 2.1.13) [37] for annotations against the non-redundant (NR) protein database and the STRING (protein-protein interaction) database; and hmmscan for Pfam domain annotation. Subsequently, functional enrichment analysis was carried out to elucidate the biological relevance of differentially expressed proteins (DEPs) or proteins of interest (POIs): GOATOOLS [38] was used for GO enrichment analysis; SciPy for KEGG enrichment analysis; and GSEA (v4.4.0) for Gene Set Enrichment Analysis—designed to identify coordinated expression changes within predefined gene or protein sets. Finally, predictions of protein structure and subcellular localization were performed to provide insights into protein function and spatial distribution: SignalP was employed to predict signal peptides, which indicates whether a protein is secretory or membrane-associated; MultiLoc for subcellular localization prediction of proteins from animals and plants.

2.12 Metabolome sample preparation and LC-MS/MS Analysis

The Liver tissue samples (25 mg ± 1 mg) were taken, mixed with beads and 500 μL of extraction solution (MeOH:ACN:H2O, 2:2:1 (v/v)). The extraction solution contains deuterated internal standards. The mixed solution was vortexed for 30 s. Then the mixed samples were homogenized (35 Hz,4 min) and sonicated for 5 min in 4 ℃ water bath, the step repeat for three times. The samples were incubated for 1 h at -40 ℃ to precipitate proteins. Then the samples were centrifuged at 12000 rpm (RCF = 13800 (×g), R =

8.6cm) for 15 min at 4 ℃. The supernatant was transferred to a fresh glass vial for analysis. The quality control (QC) sample was prepared by mixing an equal aliquot of the supernatant of samples. For polar metabolites, LC-MS/MS analyses were performed using an UHPLC system (Vanquish, Thermo Fisher Scientific) with a Waters ACQUITY UPLC BEH Amide (2.1 mm × 50mm, 1.7 μm) coupled to Orbitrap Exploris 120 mass spectrometer (Orbitrap MS, Thermo). The mobile phase consisted of 25 mmol/L ammonium acetate and 25 ammonia hydroxide in water (pH = 9.75) (A) and acetonitrile (B). The auto-sampler temperature was 4 ℃, and the injection volume was 2 μL. The Orbitrap Exploris 120 mass spectrometer was used for its ability to acquire MS/MS spectra on information-dependent acquisition (IDA) mode in the control of the acquisition software (Xcalibur, Thermo). In this mode, the acquisition software continuously evaluates the full scan MS spectrum. The ESI source conditions were set as following: sheath gas flow rate as 50 Arb, Aux gas flow rate as 15 Arb, capillary temperature 320 ℃, full MS resolution as 60000, MS/MS resolution as 15000, collision energy: SNCE 20/30/40, spray voltage as 3.8 kV (positive) or -3.4 kV (negative), respectively.

2.13 Metabolites Data preprocessing and analysis

As previously describing, the raw data were converted to the mzXML format using ProteoWizard and processed with an in-house program. which was developed using R and based on XCMS, for feature detection, extraction, alignment, and integration. The R package and the BiotreeDB (V4.0) were applied in metabolite identification. In this study, the metabolites were de-noised with relative standard deviation. The missing values were filled up by half of the minimum value. The final dataset containing the information of feature number, sample name and normalized feature area was imported to SIMCA18.0.1 software package (Sartorius Stedim Data Analytics AB, Umea, Sweden) for multivariate analysis. Data was scaled and logarithmic transformed to minimize the impact of both noise and high variance of the variables. Principle component analysis (PCA), an unsupervised analysis that reduces the dimension of the data, was carried out to visualize the distribution and the grouping of the samples. 95% confidence interval in the PCA score plot was used as the threshold to identify potential outliers in the dataset. Supervised orthogonal projections to latent structures-discriminate analysis (OPLS-DA) was applied to visualize group separation. Then, a 7-fold cross validation was performed to calculate the value of R2 and Q2. R2 indicates how well the variation of a variable is explained and Q2 means how well a variable could be predicted. The R2 and Q2 intercept values were obtained. Here, the intercept value of Q2 represents the robustness of the model, the risk of overfitting and the reliability of the model, which will be the smaller the better. Furthermore, the value of variable importance in the projection (VIP) of the first principal component in OPLS-DA analysis was obtained. It summarizes the contribution of each variable to the model. The metabolites with VIP > 1 and $p < 0.05$ (student t test) were considered as significantly changed metabolites. In addition, commercial databases including KEGG (http://www.genome.jp/kegg/) and MetaboAnalyst (http://www.metaboanalyst.ca/) were used for pathway enrichment analysis.

2.14 Cell Communication analysis

Selected a specific origin cell and, based on the Cellchat database [39], first determined the relative expression levels of ligand proteins in this type of cell. Then, we paired them with the corresponding

receptors in other types of cells. The communication strength between the origin cell and the target cell was measured by the total expression levels of ligand-receptor pairs. We analyzed the differences between the two groups (CON and CRS) and within each group, and the analysis dimensions included the number of communication receptor pairs, the strength of communication receptor pairs, the number of differential receptor pairs, and the strength of differential receptor pairs, etc. Using the CellPhone DB database [40], we further analyzed the interaction partners and ligands of each cell pair, use a heat map to quantitatively display the number of ligands for each cell pair ($P < 0.05$). Based on the results of the previous research, the functions of the ligand-receptor pair in pro-inflammatory (Pro-inf) and anti-inflammatory processes (Anti-inf) are annotated. Quantification of the relative expression levels of the ligand-receptor pairs, and determination of whether the corresponding ligand-receptor pairs are significantly different between the corresponding cell pairs based on the P-value.

2.15 Prediction of the cellular source of differential expression proteins

Obtain the single-cell sequencing data of mouse liver and the cell annotation information from the Tabula Muris database (https://tabula-muris.sf.czbiohub.org/). The single-cell sequencing of PFC and mouse retina was conducted using the data from this study. Obtain the differentially expressed proteins (Up-regulated Foldchange > 1.5, Down-regulated Foldchange < 1/1.5) in the PFC, Retina, and Liver induced by CRS. Match the differences with the cell types in the single-cell sequencing of the corresponding tissues to confirm the expression distribution of the differentially expressed proteins in different numbers of cell types and immune cell types. Select the top 10 differentially expressed proteins in each tissue for cell source display.

2.16 Inter-organ communications before and after depression

Based on the proteomic identification results of the PFC, retina, and liver, we obtained the union of the differentially expressed proteins in the three tissues (PFC, retina, and liver). These proteins were different in at least one of the tissues. Simultaneously calculate the correlations between different tissues in normal and depressed states, using the Spearman coefficient to measure the correlation between the two tissues. Visualize the correlation results of specific tissue pairs using the Cytoscape software.

2.17 Data Availability

The raw and processed scRNA-seq data generated in this study have been deposited in NCBI under accession number GSE348994, GSE348668, GSE342618, and GSE343097 (https://submit.ncbi.nlm.nih.gov/subs/). The proteomic datasets have been deposited in ProteomeXchange(http://www.ebi.ac.uk/pride) under accession number PXD082883, PXD082837, PXD082774, and PXD082868. The metabolomic datasets have been deposited in MetaboLights under accession number MTBLS15187 (https://www.ebi.ac.uk/metabolights/editor/console). Source data underlying the graphs and analyses presented in this study are provided with this Article. Other data

supporting the findings of this study are available from the corresponding author upon reasonable request.

3. Results

3.1 CRS induces depressive-like behaviors accompanied by retinal thinning

To establish a chronic stress-induced depression model, C57BL/6J mice were subjected to a 14-days CRS paradigm followed by a battery of behavioral assessments (Fig. 1A). Consistent with successful model establishment, CRS-exposed mice exhibited robust depressive-like phenotypes, including behavioral despair and anhedonia. Compared with control mice, CRS mice showed a significant reduction in sucrose preference in SPT and a marked increase in immobility time in TST, whereas no significant difference was detected in FST (Fig. 1B). In OFT, CRS mice displayed reduced total locomotor activity together with decreased time spent and distance traveled in the center zone, indicating impaired exploratory behavior and increased depressive-like phenotypes (Fig. 1C, D).

To determine whether chronic stress was associated with structural retinal alterations, we next evaluated retinal morphology using OCT and HE staining. Quantitative OCT analysis demonstrated a significant reduction in total retinal thickness, measured from the internal limiting membrane (ILM) to the retinal pigment epithelium (RPE), following CRS exposure (Fig. 1E, F). This thinning was predominantly attributable to reductions in the outer retina, particularly the ONL, although significant thinning was also observed in the inner retinal layers, including the retinal nerve fiber layer (RNFL), ganglion cell layer (GCL), inner plexiform layer (IPL), and inner nuclear layer (INL) (Fig. 1E, F).

Histological analysis corroborated the OCT findings. HE staining revealed a significant decrease in overall retinal thickness following CRS, accompanied by reduced cellularity within both the GCL and the ONL (Fig. 1G, H). Specifically, the number of RGCs and photoreceptor nuclei was significantly decreased in CRS-treated mice compared with controls. Collectively, these structural analyses demonstrate that prolonged CRS induces widespread retinal degeneration characterized by thinning of both the inner and outer retina, suggesting that chronic psychological stress compromises retinal integrity.

3.2 CRS reshapes the proteomic landscape and cellular transcriptional profiles in the PFC and Retina

To comprehensively characterize molecular alterations induced by CRS, we performed deep quantitative proteome analysis together with scRNA-seq in the PFC and retina from control and CRS-exposed mice (Fig. 2A). The principal component analysis of the PFC (Figure S1 A) and retina (Figure S1 B) proteomic datasets demonstrated clear separation between the CON and CRS groups while showing high within-group consistency, indicating robust data quality and distinct stress-induced proteomic remodeling in both tissues.

A total of 9,420 protein groups (9,484 proteins) were quantified in the PFC, whereas 9,915 protein groups (9,964 proteins) were identified in the retina (Fig. 2B, Supplementary Table 1). To determine whether CRS elicited coordinated or tissue-specific protein alterations, we performed nine-quadrant co-expression analysis of differentially expressed proteins shared between the two tissues (Fig. 2C). Most differentially expressed proteins exhibited tissue-specific regulation, with 130 proteins uniquely downregulated in the retina (Down Retina) and 98 uniquely upregulated in the PFC (Up PFC & Un Retina). In contrast, a relatively small subset of proteins displayed concordant regulation in both tissues, including 47 proteins that were simultaneously upregulated (Up PFC & Up Retina) and 7 proteins that were simultaneously downregulated (Down PFC & Down Retina), suggesting that CRS induces both common and tissue-dependent proteomic responses.

To further resolve the cellular basis underlying these molecular changes, we generated single-cell transcriptomic profiles of the PFC and retina from CON and CRS mice[39]. After stringent quality control, 101,901 cells from the PFC were retained for downstream analysis (for the CON group and the number of cells in each replicate was 14662, 14868, 13293, 13898. The number of identified cells in CRS group are 12194, 10574, 11944, 10508) (Figure S1 C, Supplementary Table 2). Unsupervised clustering identified nine major cell populations, including glutamatergic neurons, GABAergic neurons, astrocytes, oligodendrocytes, oligodendrocyte precursor cells (OPCs), microglia, endothelial cells, pericytes, and fibroblasts (Fig. 2D). Cell-type annotation was validated by canonical marker gene expression, confirming the reliability of the clustering results (FigureS2A). The overall cellular composition of the PFC was largely preserved following CRS, with the proportions of major cell populations remaining consistent between groups (FigureS1D). In contrast, differential expression analysis revealed substantial transcriptional remodeling across multiple cell types in response to chronic stress (FigureS1E, FigureS2B, Supplementary Table 3). The number of differentially expressed genes varied considerably among cell populations, indicating pronounced cell type-specific transcriptional responses to CRS (Up-regulated Foldchange > 2, Down-regulated Foldchange < 0.5, p_val_adj < 0.05).

To further characterize the cellular responses to CRS in the retina, we performed scRNA-seq of retinal tissues from control and CRS-exposed mice. A total of 74,419 retinal cells were retained for downstream analysis, for the number of cells in CON group was 9241, 8545, 9891, 7737, and those in CRS group are 9153, 8300, 10200, 11527) (Figure S1 F, Supplementary Table 4). Unsupervised clustering identified nine major retinal cell populations, including rod photoreceptors (Rod PRs), cone photoreceptors (Cone PRs), bipolar cells, Müller glia, RPE, RGCs, amacrine/horizontal cells (AC/HC), endothelial cells, and microglia (Figure S1 G). Cell identities were validated by the expression of established canonical marker genes, confirming the accuracy and robustness of cell-type annotation (FigureS2C).

The overall cellular composition of the retina remained largely comparable between the CON and CRS groups, with no substantial changes in the proportions of the major retinal cell populations (FigureS1G). However, differential gene expression analysis revealed extensive transcriptional remodeling across retinal cell types following CRS (FigureS1H, FigureS2D, Supplementary Table 5). The number of

differentially expressed genes varied considerably among individual cell populations, indicating that chronic stress elicits highly cell type-specific molecular responses within the retina.

Due to the thinning of the ONL in the depressed state, we specifically conducted differential pathway enrichment analysis for Cone PRs (FigureS2E), Rod PRs (FigureS2F), and RGCs (FigureS2G). And through the analysis of the metabolic pathways associated with PFC cell subgroups, an attempt was made to identify the common pathways through which photoreceptor cells project to PFC cells in the depressed state. The results showed that the changed pathway Tyrosine metabolism of Rod PRs most specifically projected to the Neuron Glutamatergic in PFC (Fig. 2F), Glutamatergic synapse of RGCs most specifically projected to the Endothelial in PFC (Fig. 2G). Tyrosine metabolism and IL-17 signaling pathway of Cone PRs most specifically projected to the Neuron Glutamatergic in PFC (Fig. 2H).

3.3 CRS disrupts retinal photoreceptor communication and reveals shared metabolic alterations with the PFC

The cell communication analysis was performed, to explore the changes in interactions among various cell populations in the PFC and retina during the depressive model. Comparable communication remodeling was also observed significant alterations in ligand-receptor interactions were detected among glutamatergic neurons, GABAergic neurons, astrocytes, oligodendrocytes, and OPCs following CRS (Figure S3A-D), accompanied by widespread changes in receptor abundance across these cell populations (Figure S4A-D). In a depressed state, the interaction weight/strength of GABAergic neuron subtypes and the connections between them and astrocytes, oligodendrocytes, and OPCs all significantly decrease (Figure S3E, S4E). Meanwhile, compared with the CON group, the interaction patterns among various cell populations in the retina of the depressed mice also underwent significant changes (Figure S3F-I), accompanied by widespread changes in receptor abundance across these cell populations (Figure S4F-I). The interaction intensities between RGC cells and Cone PRs, Rod PRs, Muller glia, Amacrine cells, and bipolar cells were all significantly reduced (Figure S3J, S4J). To further characterize depression-induced changes in retinal signaling, we focused on communication originating from photoreceptors. When Rod PRs were defined as sender cells, their interaction strength with Amacrine cell, Cone PRs, Müller glia, RGCs was most significantly downregulated in CRS mice (Figure S5A–C). Notably, *Sirpb1c–Cd47* signaling from Rod PRs to RGCs was significantly increased (Figure S5G), whereas *Ncam1–Ncam1*, *Ncam1–Ncam2* and *Ncam1–L1cam* signaling was markedly attenuated (Figure S4H) in CRS mouse. Similarly, Cone PRs-derived signaling toward RGCs was broadly diminished in CRS (Figure S5D–F), accompanied by mostly increased *Sirpb1c–Cd47* (Figure S5G) and mostly decreased *Negr1-Negr1* and *Ncam1-Ncam1* signaling toward RGCs (Figure S5H). In addition, the Cellphone DB analysis revealed that during the interaction process of Cone PRs-RGCs in a CRS group, the anti-inflammatory receptors showed significant changes in the expression of *CD47_SIRPA* and *GAS6_TYRO3* (Figure S5I, S5J). Together, these findings indicate that chronic stress profoundly disrupts communication between retinal photoreceptors and RGCs.

In depression model, retinal photoreceptors and brain cells also exert regulatory effects on the disease through common metabolic pathways. To determine whether retinal and prefrontal cells shared common molecular adaptations to chronic stress, we performed KEGG pathway enrichment analysis of differentially expressed genes across individual retinal and prefrontal cell types. Differentially expressed genes from Cone PRs, Rod PRs, and RGCs (Figure S2 E-G) were compared with those identified in each prefrontal cell population (Figure S6A-I). Cross-tissue pathway mapping revealed several shared metabolic and signaling pathways between retinal photoreceptors and specific prefrontal cell types. Cone exhibited the greatest overlap with the tyrosine metabolism in glutamatergic neurons, IL-17 signaling in glutamatergic neurons, astrocyte and Microglia and Neuroactive ligand signaling in GABAergic neuron (Fig. 2H). Rod PRs shared altered pathways with glutamatergic neurons, astrocytes, and fibroblasts, including viral protein interaction with viral interaction cytokine and cytokine receptor, primary immunodeficiency, and intestinal immune network for IgA production pathways (Fig. 2F). In contrast, RGCs displayed maximum overlap with Endothelial cell in PFC (Fig. 3F). Interestingly, both cone cells and rod cells exhibit co-regulation with Glutamatergic Neuron cells in the Tyrosine metabolism pathway. This suggests that the Tyrosine metabolism pathway may play an important regulatory role in the regulation of the retina and brain.

Collectively, these findings demonstrate that CRS induces coordinated remodeling of photoreceptor-mediated retinal communication and reveals convergent metabolic signatures between retinal photoreceptors and specific PFC cell populations, supporting a potential retina–PFC molecular axis during chronic stress.

3.4 Integrated proteomic analysis identifies co-ordinated molecular alterations across the liver-brain-retina axis

To investigate coordinated molecular alterations across organs following CRS, we performed cross-organ correlation analysis using quantitative proteomic datasets from PFC, retina, and liver. A total of 898 proteins were commonly identified across all three tissues and were included in subsequent analyses.

The spearman correlation analysis revealed that the PFC and retina exhibited the strongest proteomic concordance under both physiological and depressive conditions (Fig. 3A). The average correlation coefficient remained high following CRS (CON: $r = 0.712$; CRS: $r = 0.710$), indicating that the overall molecular relationship between these two tissues was largely preserved. In contrast, correlations involving the liver were more susceptible to chronic stress. Specifically, the PFC–liver correlation decreased from 0.391 to 0.344, whereas the retina–liver correlation declined from 0.374 to 0.333 following CRS (Fig. 3A), suggesting that chronic stress preferentially disrupts liver-associated molecular coordination while maintaining a strong PFC-retina relationship.

To further identify molecular signatures shared among those three organs, we conducted an association analysis between the differential proteins of the retina and the total proteins of the PFC and liver. A total of 68 retinal differential proteins were co-detected in all three tissues (Fig. 3B). Among these, 45 proteins

displayed concordant expression changes across the liver-brain-retina axis, including *Pzp, Ifit1, Orm1, Hp, C3, and Cbs*, all of which were consistently upregulated following CRS. Conversely, a smaller subset of proteins, including *Kif16b, Serpina1e, Arhgap42, Ak6*, and *Psmb10*, showed consistent downregulation across those three tissues (Fig. 3C), indicating coordinated systemic molecular responses to chronic stress. The preliminary report indicates that the C3 protein is highly expressed in the aqueous humor and retina of animal myopia models, and participates in the regulation of the intraocular inflammation-immune pathway and has closely relationship with depression [41, 42]. Meanwhile, *Cbs* regulates the production of homocysteine, which is positively correlated with the risk of depression [43]. Our research progress has confirmed that the regulation between the liver-brain-retina in the depression model exhibits a feature of consistent interaction.

To determine the retinal cellular origin of these shared molecular signatures, we examined the expression of the corresponding genes across major retinal cell populations (RGC, Cone PRs, and Rod PRs) using single-cell transcriptomic data. Among the positively correlated proteins, Mt1, Far1, H2-D1, Itih4, and Rbm3 exhibited the highest expression levels, with predominant enrichment in RGCs, followed by cone and Rod PRs (Fig. 3D). In contrast, Slc6a13, corresponding to negatively correlated proteins, was primarily expressed in RGCs, whereas Fmo5 and Serpina3n showed relatively low expression in photoreceptor populations (Fig. 3E). Herein, Mt1 emerged as a prominent molecule because of its high expression in RGCs, and regulate the circadian function of photoreceptor cells in the retinal ONL, which would further influencing the depressive-like behaviors and broad concordant regulation across the PFC, retina, and liver [44–46]. These findings identify Mt1 as a candidate molecular mediator linking retinal and central nervous system responses to chronic stress and suggest that it may contribute to coordinated alterations along the liver-brain-retina axis. The KEGG enrichment analysis of all positively correlated proteins showed that the complement and coagulation cascades pathway had the highest enrichment degree (Fig. 3F). Our research results have further revealed the consistency and heterogeneity of the interaction among the liver, brain and ocular axis in the regulation of depression.

3.5 Integrated metabolomic and single-cell analyses reveal the change of Bile secretion pathway in the liver-brain-retina axis

The disorder of liver metabolism is closely related to depression [47]. To investigate coordinated metabolic remodeling across the liver-brain-retina axis following CRS, we performed proteome and untargeted metabolomic profiling of liver from CON and CRS mice. Principal component analysis demonstrated clear separation between the two groups with high within-group reproducibility, indicating robust metabolic alterations induced by CRS (Fig. 4A). Following quality control and relative standard deviation filtering, 4,991 metabolites were identified, of which amino acid derivatives, fatty acids and conjugates, and glycerophospholipids represented the major metabolite classes (Fig. 4B). Among them, 25.95% (1295 metabolites) were amino acid derivatives, 8.78% (438 metabolites) were fatty acids and conjugates, and 5.41% (270 metabolite groups) were glycerophospholipids (Fig. 4B). Integrated analysis of liver proteomic and metabolomic datasets identified 28 significantly enriched pathways that were

consistently altered at both the protein and metabolite levels (Fig. 4C), suggesting coordinated liver metabolic remodeling in response to chronic stress.

In order to further explore whether these liver metabolic alterations were shared with specific cell populations in the retina and PFC, we integrated liver metabolomic data with KEGG enrichment analyses of differential expression gene of each cell type in the PFC (Figure S6) and retina (Figure S7). The pathways that were simultaneously most abundantly enriched in PFC and various retinal cells were Glycerophospholipid metabolism, Serotonergic synapse, and Bile secretion. In CRS model, the *Dgki* gene in the Glycerophospholipid metabolism pathway was different in most cells of the PFC and retina. Similarly, the *Ldlr* and *Abcb1a* genes in the Bile secretion pathway also exhibited similar expression characteristics. What is even more interesting is that the *Cyp1b* gene, which is located upstream and downstream of bile acid metabolism, is also enriched in pathways such as Metabolism of xenobiotics by cytochrome P450, and it also shows differential expression in various cells (Fig. 4D). The analysis of the liver protein profile revealed that, compared to the control group, the expression levels of the rate-limiting enzymes Cyp7b1 and Cyp8b1 during bile synthesis were significantly downregulated (Fig. 4E). Further analysis of the expression model correlations of genes related to bile acid metabolism in brain tissues and various cell types of the retina showed that OPCs-Rod PRs and OPCs-Amacrine cells exhibited the characteristic of co-regulation of bile acid metabolism through *Abcb1a* (Figure S9, Figure S10), while OPCs-RPE was co-regulated for bile acid metabolism through the *Ldlr* gene (Figure S9).

In order to further explore the impact of depression on the expression levels of related metabolic enzymes involved bile acid secretion, 15 proteins in the liver, PFC, and retina proteome that is annotated to be related to bile acid secretion. Next, these proteins are mapped to the Cone PRs, Rod PRs and RGC cells of the retina (*Slc22a6* and *Cyp7a1* genes not detected in the retinal cell), as well as each cell in the PFC (*Cyp7a1, Slco1a1* genes not detected in the PFC cell) (Fig. 4G, H). The analysis results show that in Rod-OPCs cells, depressive-like behaviors significantly reduced the expression of *Cyp7b*1 in OPCs (Fig. 4G), and downregulated the expression of *Slc5a1* and *Abcb1a* genes in Rod PRs (Fig. 4H). The expression levels analysis of bile acid receptor (*Itga5, Nr1h2, Nr1h3, Nr1h4, Itgb1, Chrm3, Vdr, Nr1i2, Nr1i3, S1pr2*) in photoreceptors of the retina and various types of cells in the PFC shows that depression reduced the expression level of *Nr1i3* was downregulated in OPCs induced by depression (Fig. 4I), and downregulated the expression of *Nr1h4* (Farnesoid X Receptor, FXR), *Nr1i2* and *S1pr2* both in Rod and Cone PRs, but only *Nr1i3* in Cone PRs and RGC (Fig. 4J). Meanwhile, the results of liver metabolic profiling indicated that in the depressed state, most of the intermediate metabolites (Taurodeoxycholic acid, Cholic acid 7-sulfate, Deoxycholic acid, Hyodeoxycholic acid, et al.) related to bile acid metabolism were in a significantly downregulated state (Figure S11).

Collectively, these findings identify bile secretion as metabolic pathways shared across the liver and specific retinal and cortical cell populations following chronic stress, highlighting coordinated metabolic remodeling along the liver-brain–retina axis in depressive state.

3.6 Circulating proteomics identifies candidate systemic mediators associated with the liver–brain–retina axis

Investigating organs individually can reveal detailed disease processes and even common phenotypes that are potentially susceptible to intervention. However, chronic stress induced depressive like behaviors arise via systemic interorgan crosstalk, as dysfunction within a single organ may initiate or exacerbate pathological impairments across distant tissues. Investigating organs individually can reveal detailed disease processes and even common phenotypes that are potentially susceptible to intervention. However, chronic stress induced depressive like behaviors arise via systemic interorgan crosstalk, as dysfunction within a single organ may initiate or exacerbate pathological impairments across distant tissues. In part, this may be due to depression-related alterations in blood-borne factors that mediate intercellular and organ-organ communication. Numerous serum proteins implicated in cerebral injury have been validated as diagnostic biomarkers of depressive-like phenotypes.

To identify circulating proteins associated with coordinated molecular alterations across organs, we integrated serum proteomic data with tissue proteomes (PFC and Retina-Supplementary Table 1, Liver-Supplementary Table 6) and single-cell transcriptomic datasets from the PFC, retina, and liver. UpSet analysis identified 3,315 proteins that were commonly detected across all four compartments (serum, PFC, retina, and liver) (Fig. 5A). 243 proteins co-expression in serum and liver, 75 proteins co-expression in serum and retina, 48 proteins co-expression in serum and PFC (Fig. 5A). Correlation analysis of serum-tissue co-expressed proteins revealed extensive associations between circulating proteins and tissue-specific proteomic alterations. A total of 89 proteins exhibited positive correlations with the PFC, retina, or liver (Serum_Liver 33, Serum_PFC 21, Serum_Retina 35 respectively) (Fig. 5B, 5C), whereas 97 proteins showed negative correlations (Serum_Liver 31, Serum_PFC 35, Serum_Retina 31 respectively) (Fig. 5D, 5E).

To prioritize candidate circulating mediators, we further filtered serum differential proteins using a stringent correlation threshold ($|r| \geq 0.8$), yielding 10 high-confidence candidate proteins. We separately plotted correlation diagrams for the positive and negative correlations of the 10 candidate proteins. Among these candidates, VPS26B displayed the strongest negative correlations with all three tissues pairs, and FYCO1 displayed the strongest positive correlations with all three tissues pairs (Fig. 5F). To explore their potential tissue distribution, we mapped the corresponding transcripts onto scRNA-seq datasets. VPS26B transcripts were rarely detected across cell populations in the PFC (Fig. 5G), retina (Fig. 5H, 5J), or liver (Fig. 5I). In contrast, *Fyco1* expression was highly restricted to retinal cells, with predominant expression in bipolar cells, cone PRs, and rod PRs (Fig. 5H, 5J), whereas little or no expression was detected in liver (Fig. 5H) and PFC (Fig. 5I). The classification sources of liver cells, as mentioned in the aforementioned studies (Figure S8). The analysis of the interaction network between the VPS26B, FYCO1 and proteins related to bile secretion revealed that VPS26B indirectly interacts with Abcb1a through the Slc4a3 (Fig. 5K) and the FYCO1 protein interacts with Mip, Adcy9, and Atp12a protein (Fig. 5L).

Taken together, these findings identify VPS26B and FYCO1 as candidate circulating correlate, but its functional role was not further validated.

3.7 Restoration of bile acid metabolism rescues CRS-induced depressive-like behaviors and retinal photoreceptors abnormalities

To evaluate the functional relevance of the liver-brain-retina axis identified by our integrative analyses, we focused on the Rod PRs-bile secretion-OPC pathway. CRS-exposed mice were treated with the FXR agonist INT-747 to restore bile acid homeostasis, followed by behavioral and retinal assessments. INT-747 treatment significantly ameliorated CRS-induced depressive-like behaviors, as evidenced by improved locomotor activity in OFT (Fig. 6A, 6B), increased sucrose preference in SPT (Fig. 6C), reduced immobility in TST (Fig. 6D). We next examined whether restoration of bile acid metabolism also mitigated retinal structural abnormalities. OCT imaging revealed that INT-747 significantly attenuated CRS-induced thinning of the RNFL–INL and ONL (Fig. 6D). In contrast, no significant recovery was observed in the thickness of the ONL + OPL or the total retina. As the ONL contains the nuclei of rod and cone PRs, these findings indicate that pharmacological restoration of bile acid homeostasis partially preserves retinal integrity following chronic stress, particularly within the inner retina and photoreceptor layer (Fig. 6F).

ScRNA-seq analysis was conducted on the retinas and PFCs of the depressed mice after the INT-747 intervention. The results show that INT-747, compared with CRS, increased the expression of Acnat2 in OPCs (Fig. 6G), increased the expression of *Slc27a2, Slc5a1* in Rod PRs (Fig. 6H). Meanwhile, INT-747 significantly increased the expression level of the bile acid receptor Nr1i3 in Rod PRs (Fig. 6J). Compared with the CRS group, INT-747 further reduced the expression of *Vps26b* in Amacrine cells and Endothelial cells, while up-regulating its expression in Horizontal cells, Rod PRs, RGC, Cone, and RPE (photoreceptor) cells (Fig. 6K). Furtherly, INT-747 decreased the expression of *Fyco1* in RGC and Horizontal cell, but increased the Fyco1 expression in other type cells in Retina. Our research has revealed the regulatory mechanism of bile acid metabolism in retinal photoreceptor cells on depressive-like behaviors, providing a reference for the later treatment of depression and targeting points.

4. Discussion

In our study, we identified support a model in which chronic restraint stress disrupts hepatic bile acid homeostasis, which is associated with selective vulnerability of retinal rod PRs and convergent molecular alterations in prefrontal OPCs, thereby linking peripheral metabolic remodeling with depressive-like behavior and retinal dysfunction.

Especially, leveraging integrated proteomic and single-cell transcriptomic profiling identify that rod PRs may constitute a vulnerable retinal node within the liver–brain–retina network. Our analyses reveal that depression-associated molecular perturbations are preferentially enriched in rod and cone PRs, rather

than RGCs, indicative of cell-type-selective susceptibility instead of global, non-specific retinal impairment. Photoreceptors are among the most metabolically demanding cell types in mammalian tissues, relying on continuous outer segment renewal and high basal energy turnover to sustain physiological function. This extreme metabolic dependency renders PRs inherently susceptible to systemic homeostatic and metabolic disturbances induced by chronic stress. Furthermore, the divergent molecular responses across Rods PRs, Cones PRs, and RGCs corroborate the existence of cell-type-specific adaptive and pathological retinal remodeling under stress conditions. Collectively, these findings refine the current retina–brain regulatory framework, establishing photoreceptors as key early cellular responders to systemic depression-related pathological remodeling.

A major finding of our multi-omics integration was the convergence of hepatic metabolic remodeling on bile acid-related pathways. Importantly, bile secretion and bile acid-associated pathways emerged not only in the liver metabolome/proteome but also in the molecular programs of retinal rod PRs and prefrontal OPCs. Beyond their canonical functions in nutrient absorption and cholesterol homeostasis, bile acids act as pleiotropic signaling molecules that modulate inflammatory responses, mitochondrial quality control, and cellular stress adaptation via nuclear and membrane receptors including FXR and G protein-coupled bile acid receptor (GPBAR1, TGR5). Prior studies have established that bile acid signaling regulates oligodendrocyte maturation, myelin integrity, and neuronal function, and aberrant circulating bile acid profiles have been consistently detected in MDD patient cohorts [48–52]. Extending these findings, our study demonstrates that chronic stress induces systemic metabolic disorders by inhibiting liver bile acid synthase (Cyp7b1/Cyp8b1) (Fig. 4E, 4F), with bile acid profiles and disrupts Abcb1a-mediated transport dynamics on cortical and retinal cells (Fig. 4G-J). Crucially, multi-organ correlation analysis identified Abcb1a, a master efflux transporter intrinsically tied to bile acid dynamics, as the candidate molecular mediator connecting the liver-brain-retina axis. Rather than acting merely as a passive barrier component, aberrant upregulation of Abcb1a directly contributes to affective pathology, triggering anxiety- and depressive-like behaviors [53]. Notably, the marked enrichment of dysregulated bile acid pathways and Abcb1a dysfunction in rod photoreceptors provide a precise molecular and cellular basis for the pathological crosstalk between systemic metabolic failure and stress-associated brain-retinal disorders. This cross-tissue convergence suggests that altered bile acid secretion may represent a metabolic link between peripheral hepatic dysfunction and CNS responses to chronic stress.

The convergence of bile acid-associated molecular programs in rod PRs and prefrontal OPCs raises the possibility that these two cell populations represent coordinated nodes within a liver–brain–retina response network. Studies in patients with MDD demonstrate severe prefrontal OPCs alterations, particularly characterized by a block in the differentiation of OPCs into mature myelinating oligodendrocytes, leading to compromised structural connectivity and network dysfunction [54, 55]. Concurrently, emerging evidence highlights the vulnerability of central OPCs to peripheral metabolic signals, wherein hepatic dysfunction directly alters CNS glial homeostasis. For instance, liver-derived signals, including activation of Liver X Receptor beta (LXRβ), have been shown to modulate cortical lineage progression by driving radial glial cells (RGCs) toward OPCs fates in the dorsal cortex [56]. Despite these independent insights into liver–brain crosstalk and OPCs arrests in depression, direct

inter-organ communication connecting retinal rod PRs, hepatic metabolic signaling, and central OPCs maturation has remained largely unexplored. By demonstrating a shared, bile acid-mediated molecular response across both rod PRs and prefrontal OPCs, our study provides compelling support for a long-range, multi-organ axis. This novel liver–brain–retina axis not only expands our understanding of peripheral metabolic control over CNS cell fate, but also opens up potential therapeutic avenues for restoring OPCs differentiation and neural circuit plasticity in depression.

Notably, pharmacological activation of FXR with the selective agonist INT-747 provided functional support for the involvement of bile acid homeostasis in CRS-associated pathology. Restoration of bile acid signaling was accompanied by improvements in depressive-like behaviors and attenuation of retinal structural abnormalities. INT-747 attenuated stress-related disruption of the outer retina and modulated bile acid transporters and metabolic enzymes, including Slc27a2, Sult2a8, and Cyp7b1 in rod PRs (Fig. 6E, F, H). It also altered FXR- and S1PR2-related signaling in these cells (Fig. 6J), indicating that rod PRs may respond to systemic bile acid regulation. In cortical OPCs, INT-747 reshaped receptor and transport programs involving S1pr2, Nr1h3/2 (LXRα/β), Abcc1, and Acnat2 (Fig. 6G, I). These changes may improve OPC lipid homeostasis and facilitate differentiation under chronic stress. Together, our findings suggest that INT-747 simultaneously restores retinal integrity and OPC-associated glial programs, supporting peripheral bile acid signaling as a potential therapeutic target for depression.

Besides, our cross-organ proteomic reveals a set of conserved trafficking and bile-acid handling molecules that are coherently perturbed across serum, liver, retina, and prefrontal cortex under chronic stress (Fig. 5F–J). Among these candidates, VPS26b emerged as a component of the retromer-related endosomal transport machinery, suggesting that stress may broadly affect intracellular sorting pathways linked to bile-acid–responsive transport systems. Consistently, integrative analyses further connect this regulatory axis to the bile-acid efflux–associated transporter program through Slc4a3 (Fig. 5K), implying a stress-sensitive coupling between endosomal recycling capacity and maintenance of systemic bile acid/lipid equilibrium [57]. Functionally, hepatic bile acid accumulation during chronic stress is accompanied by disrupted systemic bile-acid and lipid homeostasis, which is associated with a downstream impairment of retina barrier integrity. Together, these findings support a coordinated liver–brain–retina remodeling of bile-acid secretion and intracellular recycling pathways, contributing to PFC and retinal vulnerability under stress.

Collectively, our study uncovers a previously uncharacterized liver–brain–retina axis underlying chronic stress-induced depressive pathogenesis. Chronic stress primarily disrupts hepatic bile secretion, shifting systemic circulating bile acid/lipid homeostasis and producing blood-borne metabolic stress signals. These upstream bile acid cues converge on the retinal core response node—rod PRs—where they propagate into maladaptive endosomal/trafficking remodeling that destabilizes the blood–retina barrier and selectively sensitizes rod PRs. Within the brain-retina communication pathway, OPCs serve as the intermediate connector, translating retinal dysfunction into altered prefrontal glial/neuronal programs. Notably, our multi-organ data support that molecules such as VPS26b and Abcb1a mark this cross-talk, but the dysregulated bile acid network acts as the dominant upstream driver.

Several methodological limitations of this study require explicit acknowledgment. Although multi-omics integration and pharmacological rescue experiments validate the functional role of bile acid secretion in chronic stress-induced depression, the precise functions of specific bile acid secretion, their cognate receptors, and the downstream cellular and molecular cascades remain incompletely characterized. In addition, future studies incorporating genetic manipulation of key bile acid secretion components and independent human cohort validation are required to consolidate the clinical translational relevance of our findings. Despite these limitations, our work reveals an unanticipated mechanistic link between hepatic metabolic homeostasis and retinal vulnerability, establishing a systemic framework for understanding how peripheral metabolic perturbations drive chronic stress-related neurobiological and behavioral deficits in depression.

Abbreviations

CNS
central nervous system
CRS
chronic restraint stress
DRN
dorsal raphe nucleus
FST
Forced swimming test
INL
inner nuclear layer
IPL
inner plexiform layer
ILM
internal limiting membrane
GCL
ganglion cell layer
LXRβ
Liver X Receptor beta
MDD
major depressive disorder
OCT
Optical coherence tomography
OFT
Open field test
ONL
outer nuclear layer
OPCs

oligodendrocyte precursor cells
RGCs
retinal ganglion cells
RNFL
retinal nerve fiber layer
RPE
retinal pigment epithelium
SPT, Sucrose preference test
TST
Tail suspension test
vLGN
ventral lateral geniculate nucleus.

Declarations

Author Contributions

Conceptualization, Y.F.Z., Y.T.; methodology and investigation, Y.H.D., Y.C.C., X.Y.Y, M.Y.W., J.L.Z, Y.X, H.Z.; data curing, J.L.X., H.Z., S.Y.W; writing—original draft preparation, D.Y.H., Y.F.Z. and C.Y.C.; writing—review and editing, Y.T. J.T.S and D.N.W.; funding acquisition, Y.F.Z., and Y.T. All authors have read and agreed to the published version of the manuscript.

Acknowledgments

We sincerely appreciate Professor Jiang-Fan Chen for his insightful suggestions and revision of this manuscript.

Funding

This work was financially supported by the National Natural Science Foundation of China (82505298, 82205281). Sichuan Science and Technology Program（2026NSFSC0647, 2026NSFSC1863）, Natural Science Foundation of Hubei Province (2026AFB801) and Fujiang Scholar Talent Rsearch Capacity Enhancement Program at Sichuan College of Traditional Chinese Medicine (26FJRC02) are also gratefully acknowledged.

Competing Interests

The authors declare no competing interests.

References

1. Zhang S, et al. Advances in eye-brain axis: Anatomy, immunity, and association with visual dysfunction. *Ageing Res Rev*. 2026;113(102925. https://doi.org/10.1016/j.arr.2025.102925.

2. Zhang X, et al. Eye-brain axis: Ocular and visual pathophysiology as driver and therapeutic target across the mood disorder trajectory. *Prog Retin Eye Res*. 2026;112(101467. https://doi.org/10.1016/j.preteyeres.2026.101467.
3. Wang X, et al. An ocular glymphatic clearance system removes β-amyloid from the rodent eye. *Sci Transl Med*. 2020;12(536):https://doi.org/10.1126/scitranslmed.aaw3210.
4. Yin X, et al. Compartmentalized ocular lymphatic system mediates eye-brain immunity. *Nature*. 2024;628(8006):204–211. https://doi.org/10.1038/s41586-024-07130-8.
5. Li CY, et al. The Light-Eye-Brain Axis: Neurobiological Links Between Mood Disorders and Myopia-A Narrative Review. *Ophthalmol Ther*. 2026;15(3):901–924. https://doi.org/10.1007/s40123-026-01315-2.
6. Liu Y, et al. Factors related to retinal nerve fiber layer thickness in bipolar disorder patients and major depression patients. *BMC Psychiatry*. 2021;21(1):301. https://doi.org/10.1186/s12888-021-03270-7.
7. van der Heide FCT, et al. Association of Retinal Nerve Fiber Layer Thickness, an Index of Neurodegeneration, With Depressive Symptoms Over Time. *JAMA Netw Open*. 2021;4(11):e2134753. https://doi.org/10.1001/jamanetworkopen.2021.34753.
8. Zhang Y, et al. Quantitative Swept-Source Optical Coherence Tomography Angiography Indicators of Neurovascular Dysfunction in Alzheimer Disease. *JAMA Ophthalmol*. 2026; https://doi.org/10.1001/jamaophthalmol.2026.1986.
9. Dong C, et al. A critical overview of systematic reviews and meta-analyses of light therapy for non-seasonal depression. *Psychiatry Res*. 2022;314(114686. https://doi.org/10.1016/j.psychres.2022.114686.
10. Huang L, et al. A Visual Circuit Related to Habenula Underlies the Antidepressive Effects of Light Therapy. *Neuron*. 2019;102(1):128–142.e128. https://doi.org/10.1016/j.neuron.2019.01.037.
11. Kuo BL, et al. Evidence for the Hepato-Retinal Axis: A Systematic Review. *Ophthalmic Surg Lasers Imaging Retina*. 2024;55(10):587–596. https://doi.org/10.3928/23258160-20240524-01.
12. Sit DK, et al. Adjunctive Bright Light Therapy for Bipolar Depression: A Randomized Double-Blind Placebo-Controlled Trial. *Am J Psychiatry*. 2018;175(2):131–139. https://doi.org/10.1176/appi.ajp.2017.16101200.
13. Huang X, et al. A Comprehensive Overview of the Neural Mechanisms of Light Therapy. *Neurosci Bull*. 2024;40(3):350–362. https://doi.org/10.1007/s12264-023-01089-8.
14. Lazzerini Ospri L, et al. Light affects the prefrontal cortex via intrinsically photosensitive retinal ganglion cells. *Sci Adv*. 2024;10(13):eadh9251. https://doi.org/10.1126/sciadv.adh9251.
15. Helvacıoğlu Akyüz S, et al. The brain-eye-liver axis during spaceflight: implications of hepatic dysfunction in spaceflight associated neuro-ocular syndrome. *Life Sci Space Res (Amst)*. 2025;47(164–180. https://doi.org/10.1016/j.lssr.2025.07.001.
16. Deng T, et al. Liver-derived complement component 3 promotes the susceptibility to stress-induced depression by impairing blood-brain barrier integrity. *Mol Psychiatry*. 2026; https://doi.org/10.1038/s41380-026-03551-1.

17. Siddle M, et al. Mechanistic insights into the liver-brain axis during chronic liver disease. *Nat Rev Gastroenterol Hepatol*. 2026;23(2):166–188. https://doi.org/10.1038/s41575-025-01142-z.
18. Yan L, et al. Stress increases hepatic release of lipocalin 2 which contributes to anxiety-like behavior in mice. *Nat Commun*. 2024;15(1):3034. https://doi.org/10.1038/s41467-024-47266-9.
19. Chen YC, et al. Retina and liver fibrosis screening for patients with type 2 diabetes. *Lancet Gastroenterol Hepatol*. 2025;10(5):412–413. https://doi.org/10.1016/s2468-1253(25)00092-5.
20. Lindfors A, et al. Screening for advanced liver fibrosis due to metabolic dysfunction-associated steatotic liver disease alongside retina scanning in people with type 2 diabetes: a cross-sectional study. *Lancet Gastroenterol Hepatol*. 2025;10(2):125–137. https://doi.org/10.1016/s2468-1253(24)00313-3.
21. Mondal AK, et al. Selective transcriptomic dysregulation of metabolic pathways in liver and retina by short- and long-term dietary hyperglycemia. *iScience*. 2024;27(2):108979. https://doi.org/10.1016/j.isci.2024.108979.
22. Šoša I, et al. Metabolic Dysfunction-Associated Steatotic Liver Disease Induced by Microplastics: An Endpoint in the Liver-Eye Axis. *Int J Mol Sci*. 2025;26(7):https://doi.org/10.3390/ijms26072837.
23. Zhang X, et al. Multi-omics profiling reveals liver-retina axis in high-fat diet-induced early retinopathy. *Biochem Biophys Res Commun*. 2025;781(152516. https://doi.org/10.1016/j.bbrc.2025.152516.
24. Ma S, et al. Sustained antidepressant effect of ketamine through NMDAR trapping in the LHb. *Nature*. 2023;622(7984):802–809. https://doi.org/10.1038/s41586-023-06624-1.
25. Wang M, et al. Lateral septum adenosine A(2A) receptors control stress-induced depressive-like behaviors via signaling to the hypothalamus and habenula. *Nat Commun*. 2023;14(1):1880. https://doi.org/10.1038/s41467-023-37601-x.
26. Kim GS, et al. Single-cell analysis identifies Ifi27l2a as a gene regulator of microglial inflammation in the context of aging and stroke in mice. *Nat Commun*. 2025;16(1):1639. https://doi.org/10.1038/s41467-025-56847-1.
27. Jeffries AM, et al. Single-cell transcriptomic and genomic changes in the ageing human brain. *Nature*. 2025;646(8085):657–666. https://doi.org/10.1038/s41586-025-09435-8.
28. Hao Y, et al. Dictionary learning for integrative, multimodal and scalable single-cell analysis. *Nat Biotechnol*. 2024;42(2):293–304. https://doi.org/10.1038/s41587-023-01767-y.
29. McGinnis CS, et al. DoubletFinder: Doublet Detection in Single-Cell RNA Sequencing Data Using Artificial Nearest Neighbors. *Cell Syst*. 2019;8(4):329–337 e324. https://doi.org/10.1016/j.cels.2019.03.003.
30. Korsunsky I, et al. Fast, sensitive and accurate integration of single-cell data with Harmony. *Nat Methods*. 2019;16(12):1289–1296. https://doi.org/10.1038/s41592-019-0619-0.
31. Aran D, et al. Reference-based analysis of lung single-cell sequencing reveals a transitional profibrotic macrophage. *Nat Immunol*. 2019;20(2):163–172. https://doi.org/10.1038/s41590-018-0276-y.

32. Hu C, et al. CellMarker 2.0: an updated database of manually curated cell markers in human/mouse and web tools based on scRNA-seq data. *Nucleic Acids Res*. 2023;51(D1):D870-D876. https://doi.org/10.1093/nar/gkac947.
33. Love MI, et al. Moderated estimation of fold change and dispersion for RNA-seq data with DESeq2. *Genome Biol*. 2014;15(12):550. https://doi.org/10.1186/s13059-014-0550-8.
34. Moagi GM, et al. DIA-NN EasyFilter Workflow for the Fast and User-Friendly Critical Assessment and Visualization of DIA-NN Proteomics Analysis Outcome. *J Proteome Res*. 2026;25(6):2927–2938. https://doi.org/10.1021/acs.jproteome.5c01278.
35. Ashburner M, et al. Gene ontology: tool for the unification of biology. The Gene Ontology Consortium. *Nat Genet*. 2000;25(1):25–29. https://doi.org/10.1038/75556.
36. Aramaki T, et al. KofamKOALA: KEGG Ortholog assignment based on profile HMM and adaptive score threshold. *Bioinformatics*. 2020;36(7):2251–2252. https://doi.org/10.1093/bioinformatics/btz859.
37. Buchfink B, et al. Sensitive protein alignments at tree-of-life scale using DIAMOND. *Nat Methods*. 2021;18(4):366–368. https://doi.org/10.1038/s41592-021-01101-x.
38. Klopfenstein DV, et al. GOATOOLS: A Python library for Gene Ontology analyses. *Sci Rep*. 2018;8(1):10872. https://doi.org/10.1038/s41598-018-28948-z.
39. Jin S, et al. CellChat for systematic analysis of cell-cell communication from single-cell transcriptomics. *Nat Protoc*. 2025;20(1):180–219. https://doi.org/10.1038/s41596-024-01045-4.
40. Efremova M, et al. CellPhoneDB: inferring cell-cell communication from combined expression of multi-subunit ligand-receptor complexes. *Nat Protoc*. 2020;15(4):1484–1506. https://doi.org/10.1038/s41596-020-0292-x.
41. Deng T, et al. Liver-derived complement component 3 promotes the susceptibility to stress-induced depression by impairing blood-brain barrier integrity. *Mol Psychiatry*. 2026;31(8):4233–4246. https://doi.org/10.1038/s41380-026-03551-1.
42. Zeng L, et al. Intraocular complement activation is related to retinal vascular and neuronal degeneration in myopic retinopathy. *Front Cell Neurosci*. 2023;17(1187400. https://doi.org/10.3389/fncel.2023.1187400.
43. Qu R, et al. Characteristics of clinical manifestations and molecular genetics of inherited hyperhomocysteinemia in children and adolescents: a single center experience from China. *Front Neurol*. 2025;16(1588273. https://doi.org/10.3389/fneur.2025.1588273.
44. Avelar RA, et al. A multidimensional systems biology analysis of cellular senescence in aging and disease. *Genome Biol*. 2020;21(1):91. https://doi.org/10.1186/s13059-020-01990-9.
45. Ferrucci L, et al. Measuring biological aging in humans: A quest. *Aging Cell*. 2020;19(2):e13080. https://doi.org/10.1111/acel.13080.
46. Tian YE, et al. Heterogeneous aging across multiple organ systems and prediction of chronic disease and mortality. *Nat Med*. 2023;29(5):1221–1231. https://doi.org/10.1038/s41591-023-02296-6.

47. Zhang R, et al. Social Support and Emotional Eating in Adults with Metabolic Dysfunction-Associated Fatty Liver Disease: The Chain Mediation Effects of Weight Self-Stigma and Depression. *J Multidiscip Healthc*. 2026;19(613832. https://doi.org/10.2147/JMDH.S613832.
48. Li XY, et al. TGR5-mediated lateral hypothalamus-dCA3-dorsolateral septum circuit regulates depressive-like behavior in male mice. *Neuron*. 2024;112(11):1795–1814 e1710. https://doi.org/10.1016/j.neuron.2024.02.019.
49. Limon ID, et al. Disturbance of the Glutamate-Glutamine Cycle, Secondary to Hepatic Damage, Compromises Memory Function. *Front Neurosci*. 2021;15(578922. https://doi.org/10.3389/fnins.2021.578922.
50. Romero-Ramirez L, et al. Emerging Roles of Bile Acids and TGR5 in the Central Nervous System: Molecular Functions and Therapeutic Implications. *Int J Mol Sci*. 2024;25(17):https://doi.org/10.3390/ijms25179279.
51. Sonoda Y, et al. Ursodeoxycholic acid alleviates multiple sclerosis via TGR5-dependent microglial regulation in mice. *Eur J Pharmacol*. 2025;1003(177941. https://doi.org/10.1016/j.ejphar.2025.177941.
52. Wang P, et al. Schisandrol B alleviates depression-like behavior in mice by regulating bile acid homeostasis in the brain-liver-gut axis via the pregnane X receptor. *Phytomedicine*. 2025;137(156340. https://doi.org/10.1016/j.phymed.2024.156340.
53. Wu Y, et al. Deoxycholic acid promotes anxiety- and depression-like behaviors in mice via modulation of the gut microbial metabolite indole-3-propionic acid. *Front Immunol*. 2026;17(1840574. https://doi.org/10.3389/fimmu.2026.1840574.
54. Huang C, et al. Myelin-associated oligodendrocytic basic protein-dependent myelin repair confers the long-lasting antidepressant effect of ketamine. *Mol Psychiatry*. 2024;29(6):1741–1753. https://doi.org/10.1038/s41380-023-02288-5.
55. Nagy C, et al. Single-nucleus transcriptomics of the prefrontal cortex in major depressive disorder implicates oligodendrocyte precursor cells and excitatory neurons. *Nat Neurosci*. 2020;23(6):771–781. https://doi.org/10.1038/s41593-020-0621-y.
56. Xu P, et al. Liver X receptor beta is essential for the differentiation of radial glial cells to oligodendrocytes in the dorsal cortex. *Mol Psychiatry*. 2014;19(8):947–957. https://doi.org/10.1038/mp.2014.60.
57. Wang H, et al. NEK1-mediated retromer trafficking promotes blood-brain barrier integrity by regulating glucose metabolism and RIPK1 activation. *Nat Commun*. 2021;12(1):4826. https://doi.org/10.1038/s41467-021-25157-7.

Figures

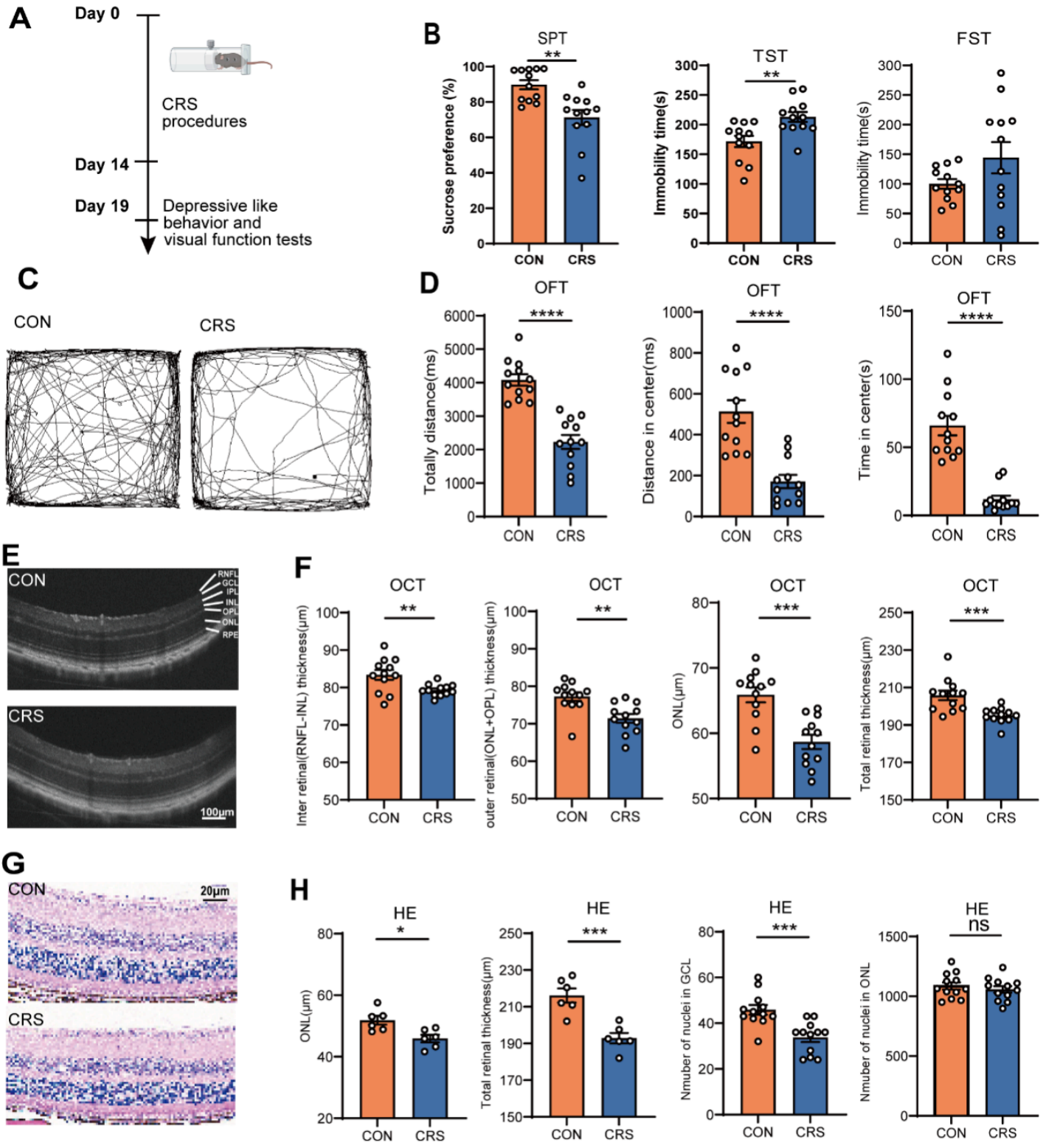


Figure 1

CRS induces depressive like behavior and retinal thinning. (A) procedures of depressive like behavior and retinal structure test. (B) CRS significantly significant sucrose preference in the SPT and a significant increase in immobility time in the TST, but not in the FST (n = 12/group, Student's t-test; t (22) = 3.740, p = 0.006; t (22) = -3.102, p = 0.005; t (13.087) = -1.607, p = 0.132). (C) Travel track visualization in Open Field Test. (D) CRS significantly decreased the totally distance, distance and time in center. (n =

12/group, Student’s t-test; t (21.192) = 6.865, p = 0.000; t (22) = 5.334, p = 0.000; t (22) = 7.080, p = 0.000). (E)Representative image of retinal OCT in control and CRS mice. (F) 14-day exposure significantly reduced inter retinal (RNFL-INL), outer retinal (ONL+OPL), ONL, and total retinal thickness. (n = 12/group, Student’s t-test; t (13.614) = 2.938, p = 0.011; t (22) = 3.529, p = 0.002; t(21.935) = 4.563, p = 0.000; t (15.785) = 3.835, p = 0.001). (G) Representative image of retinal HE staining in control and CRS mice. (H) 14-day exposure significantly reduced ONL and total retinal thickness, and induce photoreceptor cell apoptosis in GCL but not ONL (n = 12/group, Student’s t-test; t (22) = 3.300, p = 0.003; t (22) = 2.786, p = 0.011; t (21.905) = 4.160, p□0.001; t (21.830) = 0.698, p = 0.493). ^{ns}□0.05□*P < 0.05, **P < 0.01, ***P < 0.001. The data are Mean ± SEM.

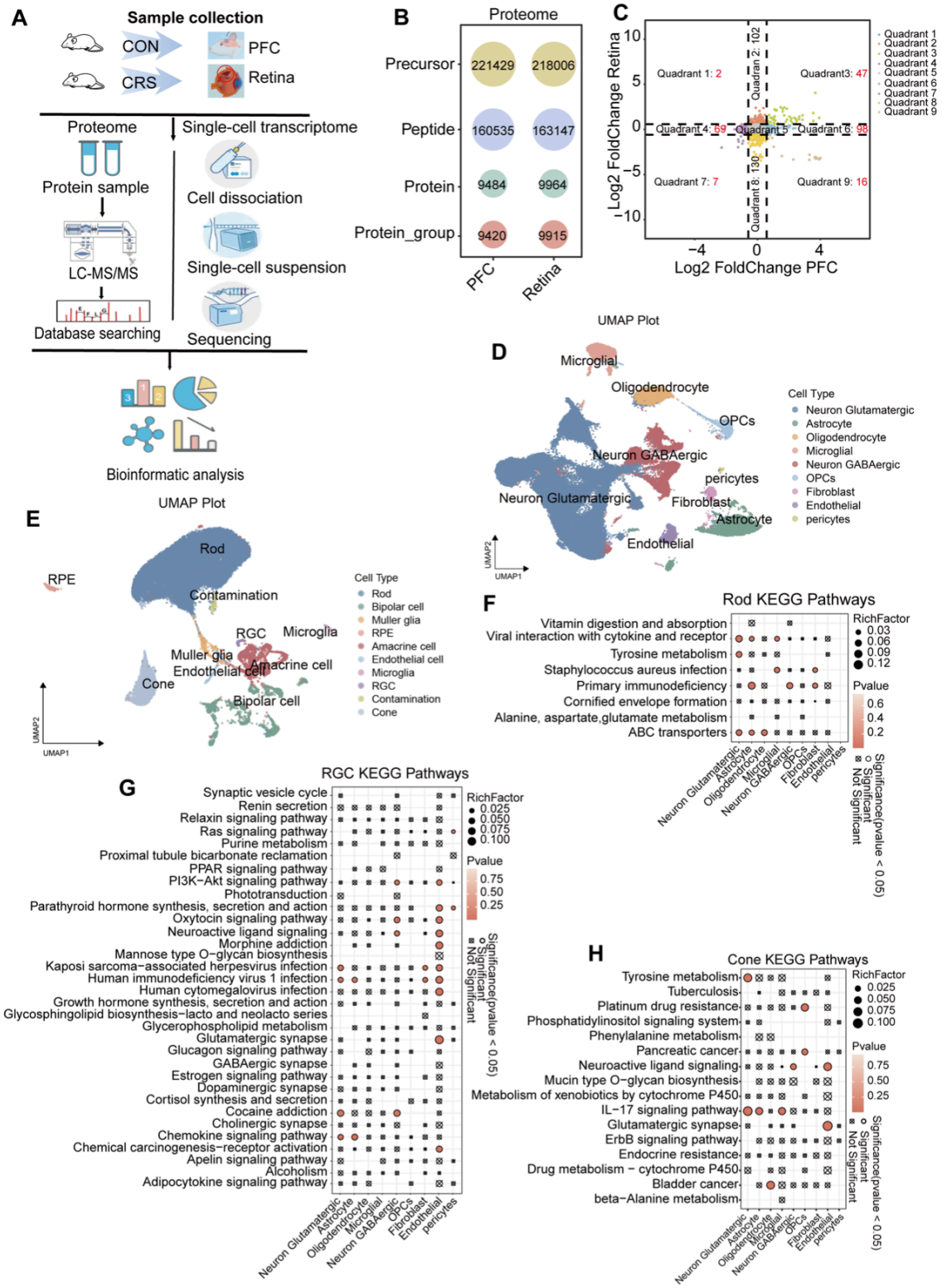


Figure 2

The proteome and single-cell sequencing profiling of PFC and Retina induced by CRS. (A) The experimental flowchart of the proteome and single-cell sequencing research of PFC and Retina. (B) Statistical analysis of the proteome data on PFC and Retina, Bubble chart showing the number of precursors, peptide, protein of PFC and Retina identified by 4D MS. (C) The 9-quadrant correlation analysis of differentially expressed proteins between PFC and Retina (Up regulated Foldchange > 1.5,

Down regulated Foldchange < 1/1.5) that show the consistency of the common differential proteins between PFC and Retina. (D) Two-dimensional Uniform Manifold Approximation and Projection (UMAP-1and UMAP-2) representation of 101,901 cell isolated from the PFC of CON and CRS induced mice. The cells are coloured based on the annotated cell type. (E) Two-dimensional Uniform Manifold Approximation and Projection (UMAP-1and UMAP-2) representation of 74,419 cell isolated from the Retina of CON and CRS induced mice. The cells are coloured based on the annotated cell type. (F, G, H) The KEGG pathways that were significantly enriched in Cone PR, Rod PR and RGC cells (p value < 0.05 & FoldEnrichment > 1.5 & count >= 2) were mapped in the differential gene enrichment pathways of each cell type in the PFC tissue (significant pathways were identified as those with p value < 0.05), (F) Rod PR map each cell type of PFC, (G) RGC map each cell type of PFC, (H) Cone PR map each cell type of PFC.

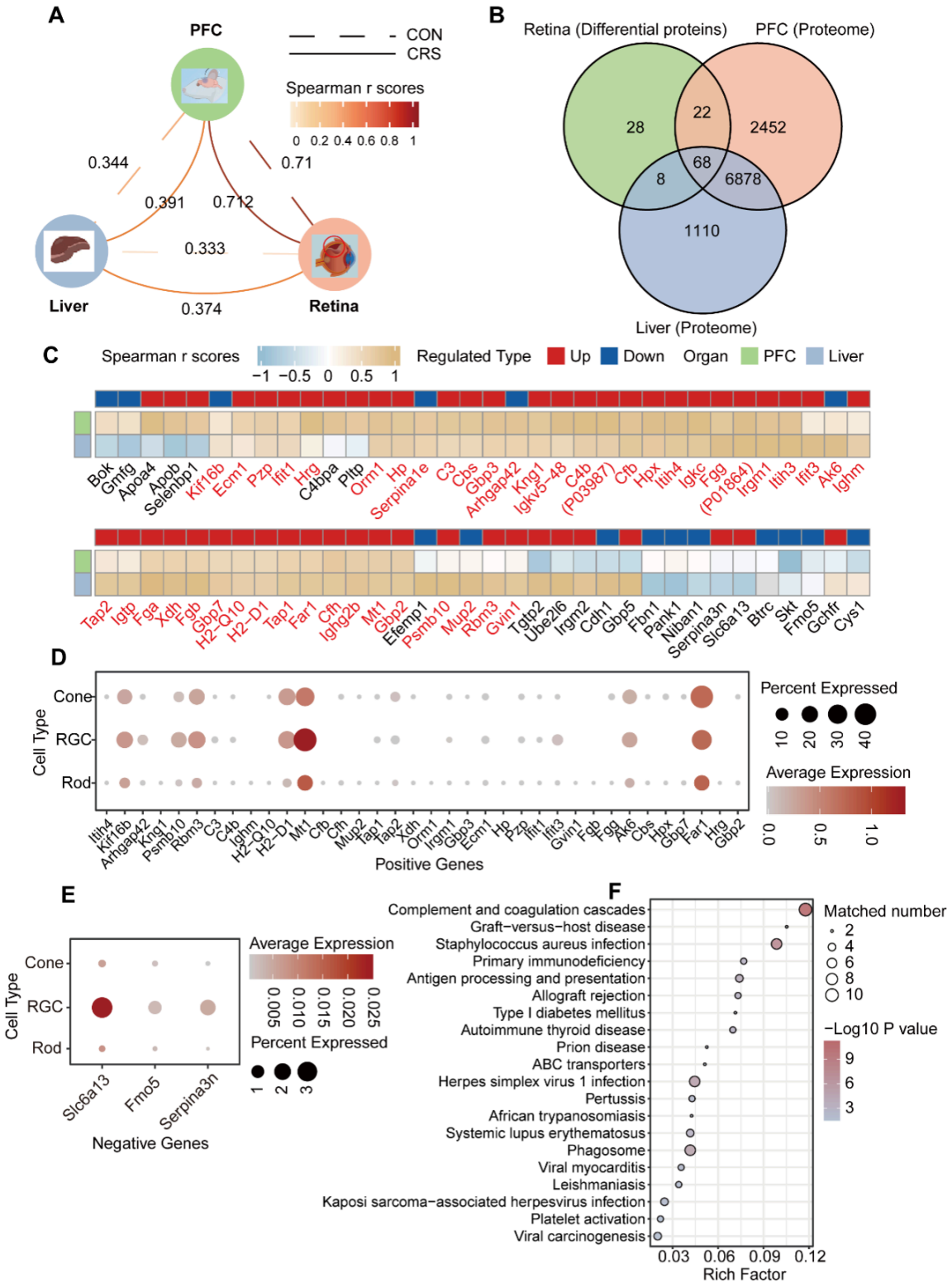


Figure 3

The interaction of liver-brain-retinas axis. (A) Influence of depression on the correlation of organs. Links are shown for the Spearman's correlation coefficient between organs (ρ > 0.3), which represents the differential expression correlation between organs in CRS and Con groups, respectively. (B) Venn diagram analysis of differentially expressed proteins (Foldchange >1.5 or <1/1.5, P<0.05) in Retina and Liver proteome, as well as PFC proteome. (C) The consistency analysis of 68 differentially expressed

proteins that are co-expressed with Liver and PFC reveals the expression regulation trends of these proteins in the Liver and PFC. The expression regulation trend of these proteins between the Liver and PFC were measured by Spearman r scores. (D) The expression analysis of positive proteins (Spearman r Scores > 0 both in Liver and PFC) in Cone PRs, Rod PRs and RGC cells. (E) The expression analysis of negative proteins (Spearman r Scores < 0 both in Liver and PFC) in Cone PRs, Rod PRsand RGC cells. (F) The KEGG enrichment of consistency expression protein (Spearman r scores > 0) from Figure 4C and 4D. The count number of matching genes in each pathway is represented by "Match number", and the size of the circle indicates the number of matching genes. The enrichment degree of each pathway is represented by the -Log10 of the P value.

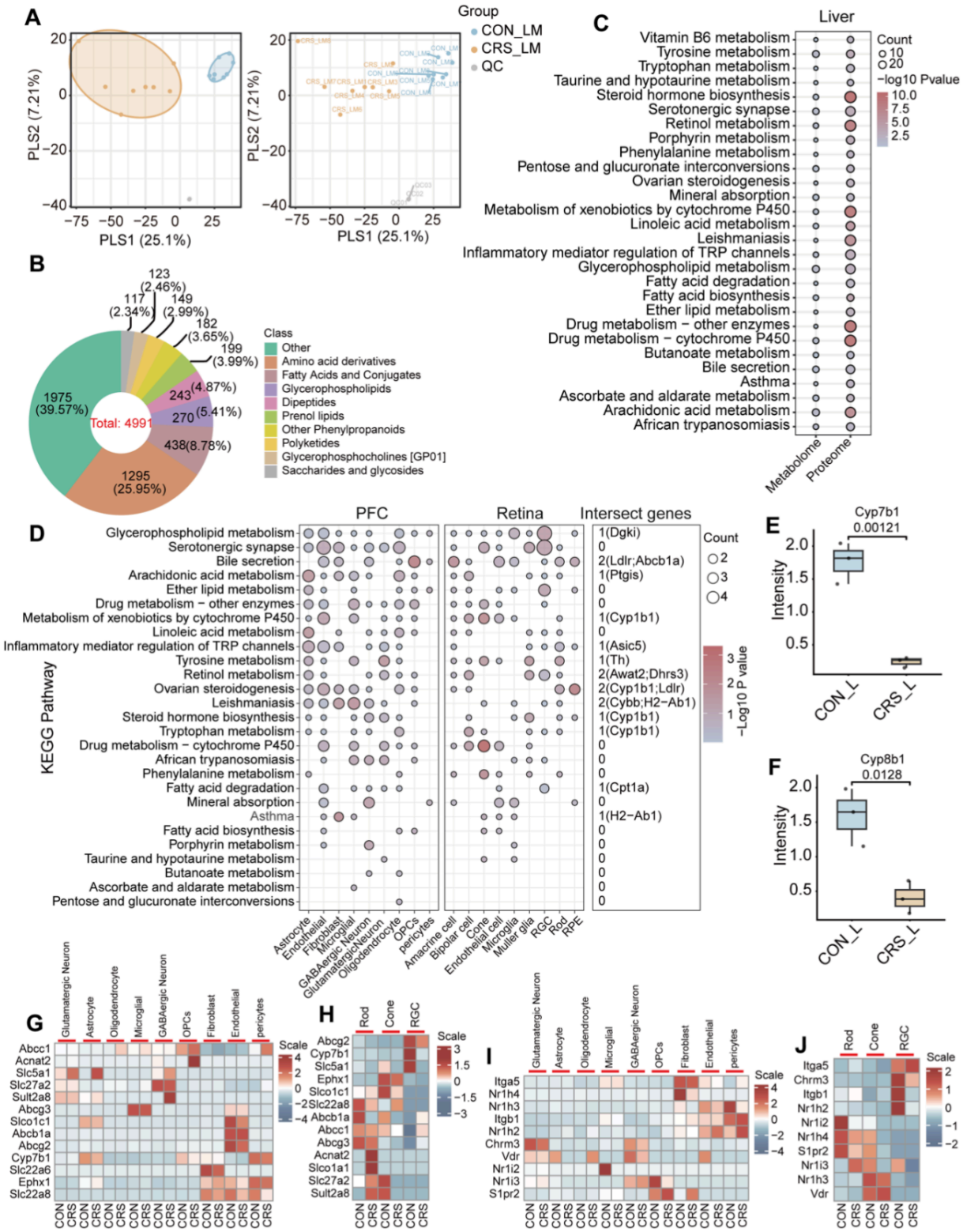


Figure 4

Analysis of common cellular metabolic pathways in the liver-brain-retina axis. (A) Principal component analysis (PCA) quality control plot of the Liver non-targeted metabolome in the Con group and the CRS group. (B) Pie chart for the classification and statistics of metabolites in the Liver metabolome. (C) Enrichment analysis of common KEGG pathways between Liver proteome and Liver metabolome. Set a threshold for proteome pathway enrichment (FoldEnrichment > 1.5, P < 0.05, Count >= 2). (D) The

consistency correlation analysis of the KEGG enrichment pathways (from Figure 4C) in each type cell of PFC and Retina. The size of the circle represents the number of common differentially expressed genes of the corresponding cell in the respective pathway, and the depth of the color indicates the significance of the difference measured by the P-value. (E-F) The expression levels of Cyp7b1 (E) and Cyp8b1 (F) proteins in the Liver. (G-H) The expression analysis of genes related to bile secretion in the cells of the PFC (G) and retinal photoreceptor cells (H). (I-J) The expression analysis of bile acid receptors related to bile secretion in the cells of the PFC (I) and retinal photoreceptor cells (J) and. The "Scale" value represents the z-score within the rows of the heatmap. The heatmap values are calculated based on the expression levels of each gene within each row, and are the row-wise Z-scores. Scale value represents the relative expression level of the gene.

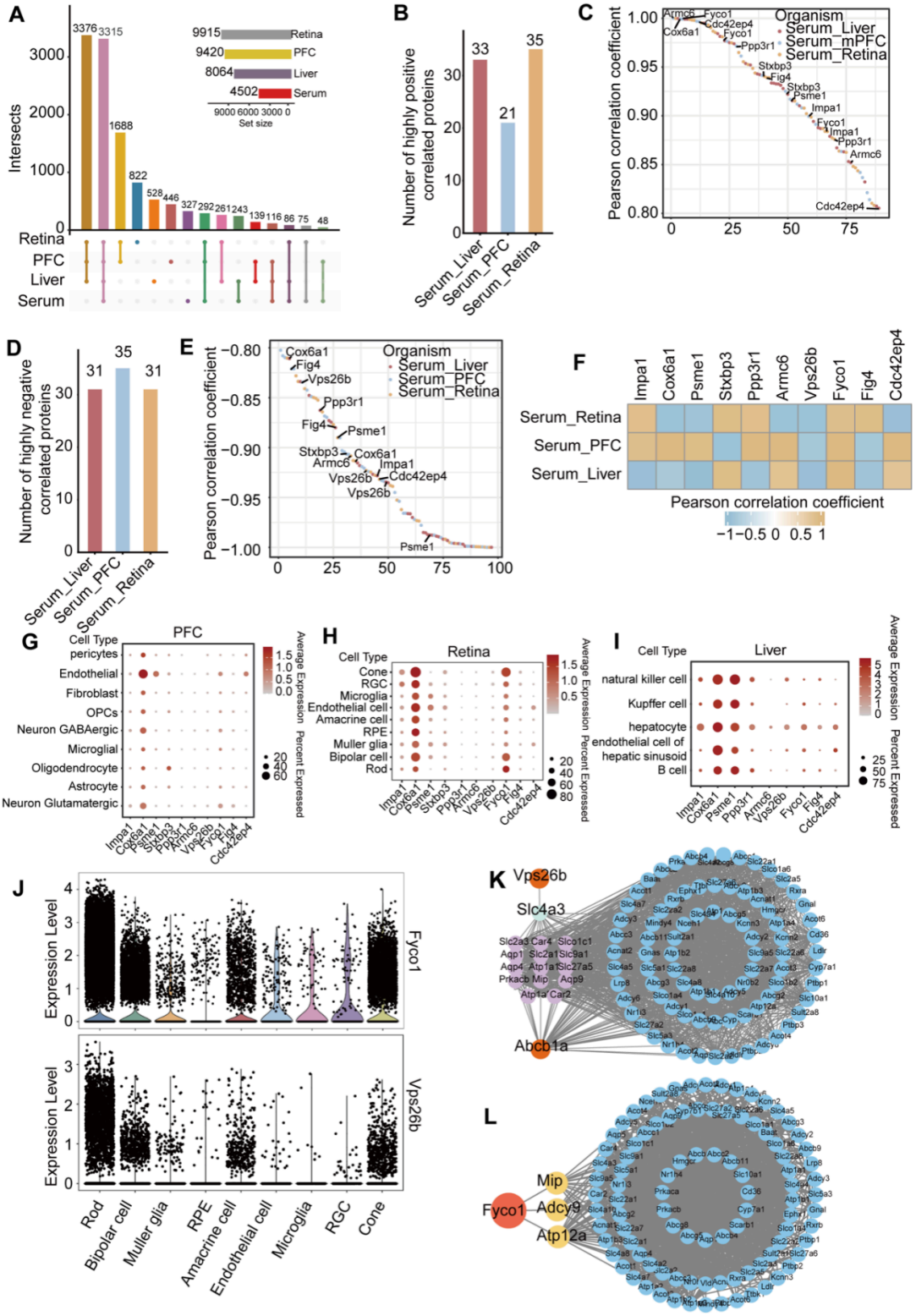


Figure 5

Correlation of plasma proteins with organ-specific gene expression. (A) The Up-Set analysis of proteome results from Serum, Liver, Retina, and PFC tissues revealed the cross-organ co-expression protein map. (B) The protein column chart analysis shows the situation of proteins in the serum differential proteins that have a positive correlation (correlation coefficient > 0.8) with the protein of PFC, Retina and Liver in the CRS group. (C) The scatter diagram shows the proteins that are positively

correlated (correlation coefficient > 0.8) with the serum differential proteins and the total proteins of PFC, Retina, and Liver in CRS group. (D) The protein column chart analysis shows the situation of proteins in the serum differential proteins that have a negative correlation (correlation coefficient < -0.8) with the protein of PFC, Retina and Liver in the CRS group. (E) The scatter diagram shows the proteins that are negatively correlated (correlation coefficient < -0.8) with the serum differential proteins and the total proteins of PFC, Retina, and Liver in CRS group. (F) The heatmap shows the proteins in Serum-PFC, Serum-Retina, and Serum-Retina paired samples that exhibit positive (correlation coefficient > 0.8) and negative correlation (correlation coefficient < -0.8) trends. These proteins showed a consistent trend in at least two of the tissue samples. (G-I) The cellular source was predicted using the scRNA-seq data, PFC (G), Retina (H), Liver (I). The interest proteins were from Figure 5F. Dot size indicates average expression (bigger = higher), while color represents the percentage of expression in cell clusters (redder = higher). (J) Expression levels of the Fyco1 and Vps26b gene in 9 types of Retinal cells (Rod, Cone, Bipolar cell, Muller glia, RPE, RGC, AC or HC, Endothelial, Microglia). (K) The interaction network of FYCO1, Vps26b protein between the proteins related to bile secretion (minimum required interaction score: 0.150).

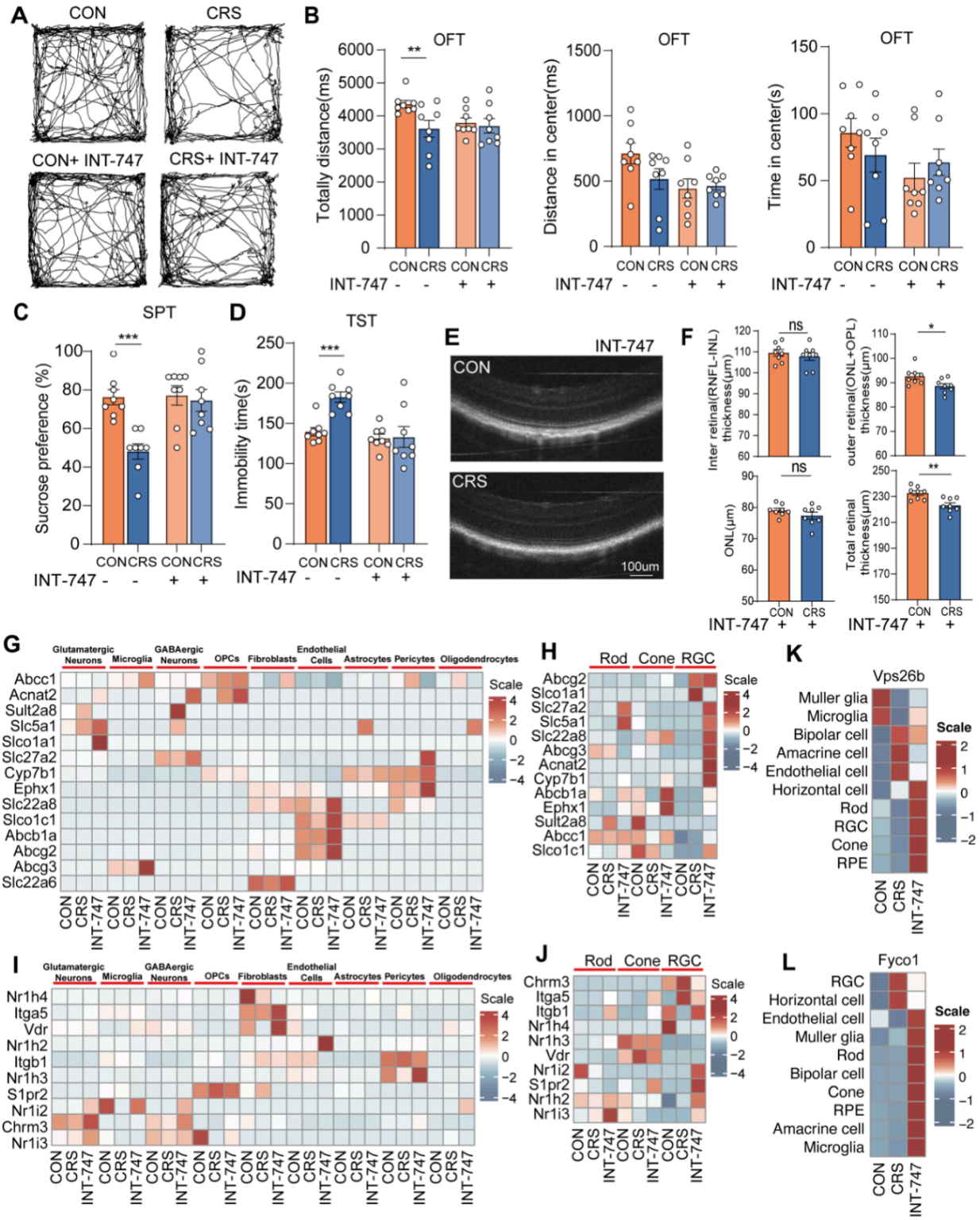


Figure 6

Restoration of bile acid metabolism rescues CRS-induced depressive-like behaviors and retinal photoreceptors abnormalities. (A) Travel track visualization in Open Field Test. (B) INT-747 injection significantly rescued totally distance, but didn't influence distance and time in center in the OFT (n = 8/group, One-way ANOVA, (F (3, 28) =3.138, P=0.041; F(3,28) = 3.183, P=0.039; F(3,28) = 1.597, P=0.212). (C, D) INT-747 injection significantly rescued sucrose preference in the SPT (C) and immobility time in the

TST (D) (n = 8/group, One-way ANOVA, F (3,28) =8.796, P<0.001; F (3, 28) =9.118, P<0.001). (E)Representative image of retinal OCT in control and CRS mice injected INT-747. (F) INT-747 injection significantly alleviated CRS-induced retinal thinning in the RNFL-INL and ONL layers, while exerting no obvious effects on ONL+OPL thickness or total retinal thickness. (n = 8/group, Student's t-test; t (14) = 0.693, p = 0.500; t (14) = 2.499, p = 0.025; t (14) = 1.322, p = 0.207; t (14) = 3.686, p = 0.002). (G-H) The expression analysis of genes related to bile secretion in the cells of the PFC (G) and retinal photoreceptor cells (H), after treated with INT-747. (I-J) The expression analysis of bile acid receptors related to bile secretion in the cells of the PFC (I) and retinal photoreceptor cells (J), after treated with INT-747. (K-L) The expression levels of the Vps26b and Fyco1 genes in various types of cells in the retina, after treated with INT-747. The "Scale" value represents the z-score within the rows of the heatmap. The heatmap values are calculated based on the expression levels of each gene within each row, and are the row-wise Z-scores. Scale value represents the relative expression level of the gene.

Supplementary Files

This is a list of supplementary files associated with this preprint. Click to download.

- 20261104Supplementaryfigures.docx
- Supplementarytable20261104.zip